Bull. Mater. Sci., Vol. 35, No. 3, June 2012, pp. 425–431. © Indian Academy of Sciences.

Electrical properties of $Sr_xBa_{1-x}Fe_{0.6}Sn_{0.4}O_{3-\varepsilon}$ NTC thermistors

C L YUAN[a,b,*], X Y LIU[a,b], J W XU[a], X W ZHANG[a] and C R ZHOU[a]

[a]School of Material Science and Engineering, Guilin University of Electronic Technology, Guilin 541004, Guangxi, China
[b]College of Materials Science and Engineering, Central South University, Changsha 410083, China

MS received 11 Feruary 2011; revised 14 July 2011

Abstract. Polycrystalline thermistor ceramics with the stoichiometric formula, $Sr_xBa_{1-x}Fe_{0.6}Sn_{0.4}O_{3-\varepsilon}$ ($0{\cdot}2 \leq x \leq 0{\cdot}8$), had been prepared by a standard solid state reaction route. X-ray diffraction analysis indicates that the ceramic system remains cubic perovskite structure with a very small lattice change. The electrical properties of $Sr_xBa_{1-x}Fe_{0.6}Sn_{0.4}O_{3-\varepsilon}$ thermistors were studied using a digital thermometer over a wide range of 298–400 K. The thermistors showed an excellent negative temperature coefficient (NTC) thermistor behaviour. The values of resistivity at 298 K (ρ_{298}), thermistor constant ($B_{298/358}$) and activation energy (E_a) of the $Sr_xBa_{1-x}Fe_{0.6}Sn_{0.4}O_{3-\varepsilon}$ thermistors, decreasing with the increase of Sr content, were in the range of 0·37–11·0 kΩ·cm, 2466–3703 K and 0·212–0·319 eV, respectively. For the thermistors with the compositions $x = 0{\cdot}2$ and 0·4, the fitting equivalent circuit was composed of three RCPE elements corresponding to grain, grain boundary and ceramic–electrode interface, respectively. From the impedance plots, it was found that the fitting data showed good agreement with the experimental data. The extracted grain boundary resistance exhibited a NTC thermistor behaviour.

Keywords. $Sr_xBa_{1-x}Fe_{0.6}Sn_{0.4}O_{3-\varepsilon}$; NTC thermistors; electrical properties.

1. Introduction

$BaSnO_3$ is an important perovskite material due to its low permittivity, semiconducting behaviour and high thermal stability. An appropriate doping in $BaSnO_3$ is expected to lead to a substantial modification in its lattice structure, defect energies, electronic disorder, redox behaviour, thermal stability and semiconducting properties, making it suitable for a variety of applications such as sensors, thermally stable ceramic capacitors (Cerdà *et al* 2002; Maekawa *et al* 2006; Kocemba *et al* 2007). The substitutions of Sr, Ca and rare earth cations for Ba in $BaSnO_3$ have already been reported (Kumar *et al* 2005a, 2006a; Hadjarab *et al* 2008). The effect of Sn-site replacement in $BaSnO_3$ by some metals such as Te, Sb, Fe and Pb has been reported and the changes in the physical properties of modified $BaSnO_3$ have also been reported (Lu *et al* 2000; Kumar *et al* 2005b, 2006b). The above literatures reveal that various aspects of physical properties such as microstructures, conduction and dielectric behaviour of modified $BaSnO_3$ have already been studied extensively.

In our previous study, we found that the $BaFe_xSn_{1-x}O_{3-\varepsilon}$ ceramic showed NTC characteristics (Yuan *et al* 2010). Now, we try to study the effect of strontium (Sr) as dopant at Ba-site on the physical properties of $BaFe_{0.6}Sn_{0.4}O_{3-\varepsilon}$. A variation of the dopant concentration is expected to cause substantial changes in the electrical properties because of the relative difference in the cation size. Furthermore, in order to have a complete understanding for the conduction mechanism, it is necessary to analyse the contributions such as grain, grain boundary and ceramic–electrode interface, to the total electrical resistance. For this purpose, we have employed complex plane impedance and modulus analysis.

2. Experimental

The ceramic phases of $Sr_xBa_{1-x}Fe_{0.6}Sn_{0.4}O_{3-\varepsilon}$ ($x = 0{\cdot}2$, 0·4, 0·5, 0·6 and 0·8) were synthesized in two steps. Intimate mixtures of $BaCO_3$, $SrCO_3$, Fe_2O_3 and SnO_2 (purity>99·9%) were weighed in stoichiometric proportions and heated in high-alumina crucibles at 1200°C for 6 h. The powders were manually ground again, pressed into cylindrical disc having 18 mm diameter and 1·5 mm thickness at 150 MPa. The discs were sintered in an air atmosphere at 1280–1300°C for 2 h, and then polished with fine emery paper to make their faces flat and parallel. The discs were finally coated with conductive silver paint and dried at 550°C for 40 min before carrying out resistivity–temperature measurements.

X-ray diffraction (XRD) data were obtained in a wide range of Bragg angles (2θ) (20–80°) at a scan speed of 6°/min by an X-ray diffractometer using Cu Kα radiation at room temperature. The surface morphologies/microstructures of the ceramics were analysed by high-resolution scanning electron microscopy (SEM) equipped

*Author for correspondence (ycgluet@yahoo.com)

with an energy-dispersive X-ray analyser (EDS). The samples of each composition were prepared for measuring electrical resistance. The samples were held with a holder in a tube furnace and their temperatures were measured with a digital thermometer. The electrical resistance of the samples in the furnace was measured with a digital multimeter (Fluke 45) from 298 to 400 K in a step of 10 K. The accuracy of the furnace measurements was ± 0·5 K.

The complex impedance spectra of the samples were measured using Agilent Impedance Analyser (4294A) controlled by a personal computer over a frequency range of 40 Hz–110 MHz. The impedance measurement of composition $x = 0{\cdot}4$ was carried out from 303 to 343 K at a temperature interval of 5 K. The heating rate was 1 K min^{-1}, while the stabilization time between consecutive measurements was 5 min. The impedance data were plotted in the complex plane, a plot of the real component vs the imaginary component. The measured samples were placed in a sample holder with a two-electrode configuration.

3. Results and discussion

From figure 1, powder XRD patterns of Sr-substituted materials have been observed to be similar to that of $BaSnO_3$ except for a very small shift in the peak positions. Preliminary structural analysis has indicated that the unit cell of $Sr_xBa_{1-x}Fe_{0{\cdot}6}Sn_{0{\cdot}4}O_{3-\varepsilon}$ remains cubic with a significant change in the lattice parameter (a) depending on Sr concentrations (inset of figure 1). Considering the $BaFe_{0{\cdot}6}Sn_{0{\cdot}4}O_{3-\varepsilon}$ perovskite cell, Sr is assumed to substitute on the A-site of the ABO_3 perovskite lattice. The substitution of Sr^{2+} for Ba^{2+} induces a small decrease of the lattice parameter (a). The decrease is in agreement with the difference of ionic radius of Sr^{2+} and Ba^{2+} (1·44 Å and 1·61 Å, respectively). Some splitting peaks are found at higher diffraction angle. According to the XRD analysis, the splitting peaks are from the contribution of $K\alpha_2$. Furthermore, there are a few weak diffraction peaks at angles 28–33°, which are related to the phases $BaFe_2O_4$, SnO_2 and SnO.

Microstructural observations further confirm the obtaining of simple perovskite phase. One of SEM micrographs obtained from the surfaces of the samples is given in the inset of figure 2 (composition with $x = 0{\cdot}8$). It is seen that uniformly sized grains are formed during sintering. The amount of porosity is very less, which denotes a dense microstructural formation. Single-phase, homogeneous, fine-grained ceramics with sufficient density are the most advantageous for practical applications. The grain size of the sample has been estimated in the range of 3–4·5 μm and the grain boundaries are observed clearly amongst the particles.

For all the samples, the compositional distribution was measured by EDS and one of the EDS analysis (for composition with $x = 0{\cdot}8$) is shown in figure 2. From figure 2, it is observed that the sample is mainly composed of elements Sr, Ba, Fe, Sn and O. Based on the EDS analysis of the samples, the calculated atomic ratio and $3-\varepsilon$ value were listed in table 1. From the table, it is seen that the $3-\varepsilon$ values are below 2·875. Thus, it is possible to postulate the following general formula for the solid solutions:

$$Sr_xBa_{1-x}\left(Fe^{3+}_{2ey}Fe^{4+}_{y-2ey}Sn^{4+}_{1-y}\right)O_{3-ey}, \quad (1)$$

where ey stands for the oxygen vacancy (ε), to maintain the equilibrium valence.

For all the compositions, d.c. electrical resistance of $Sr_xBa_{1-x}Fe_{0{\cdot}6}Sn_{0{\cdot}4}O_{3-\varepsilon}$ cylindrical discs with a diameter of about 14 mm and a height of about 1·2 mm were measured. Figure 3a shows the relationship between the electrical resistivity (ρ) and the absolute temperature. The resistivity of all the compositions decreases exponentially with increasing temperature. These measurements were also plotted in figure 3b as resistivity (ρ) as a function of reciprocal of absolute

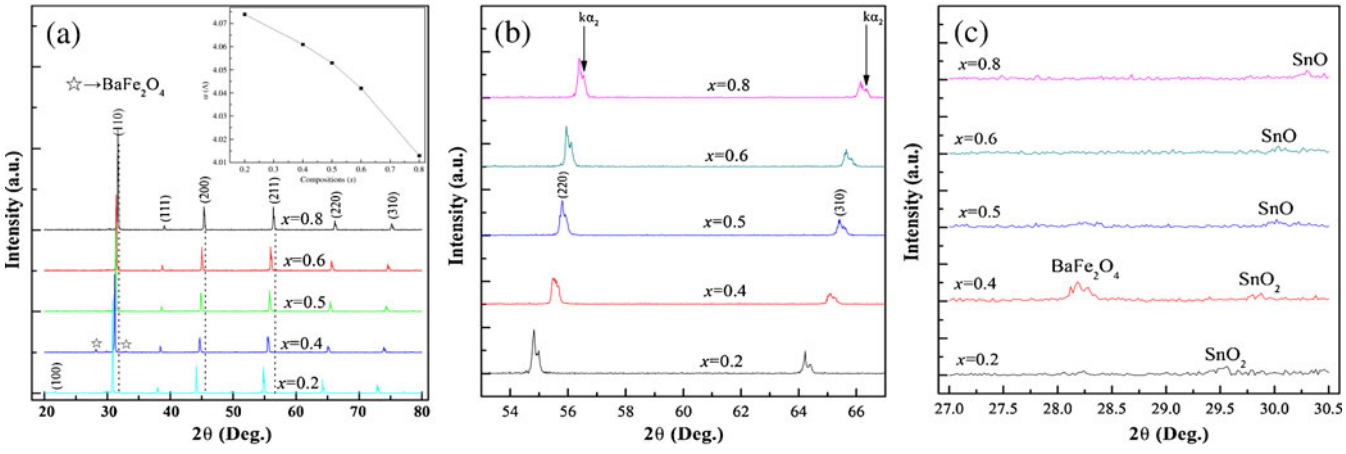

Figure 1. XRD patterns of $Sr_xBa_{1-x}Fe_{0{\cdot}6}Sn_{0{\cdot}4}O_{3-\varepsilon}$ sintered at 1280−1300°C for 2 h. Inset represents lattice parameter, a evolution vs compositions (x) in the system of $Sr_xBa_{1-x}Fe_{0{\cdot}6}Sn_{0{\cdot}4}O_{3-\varepsilon}$.

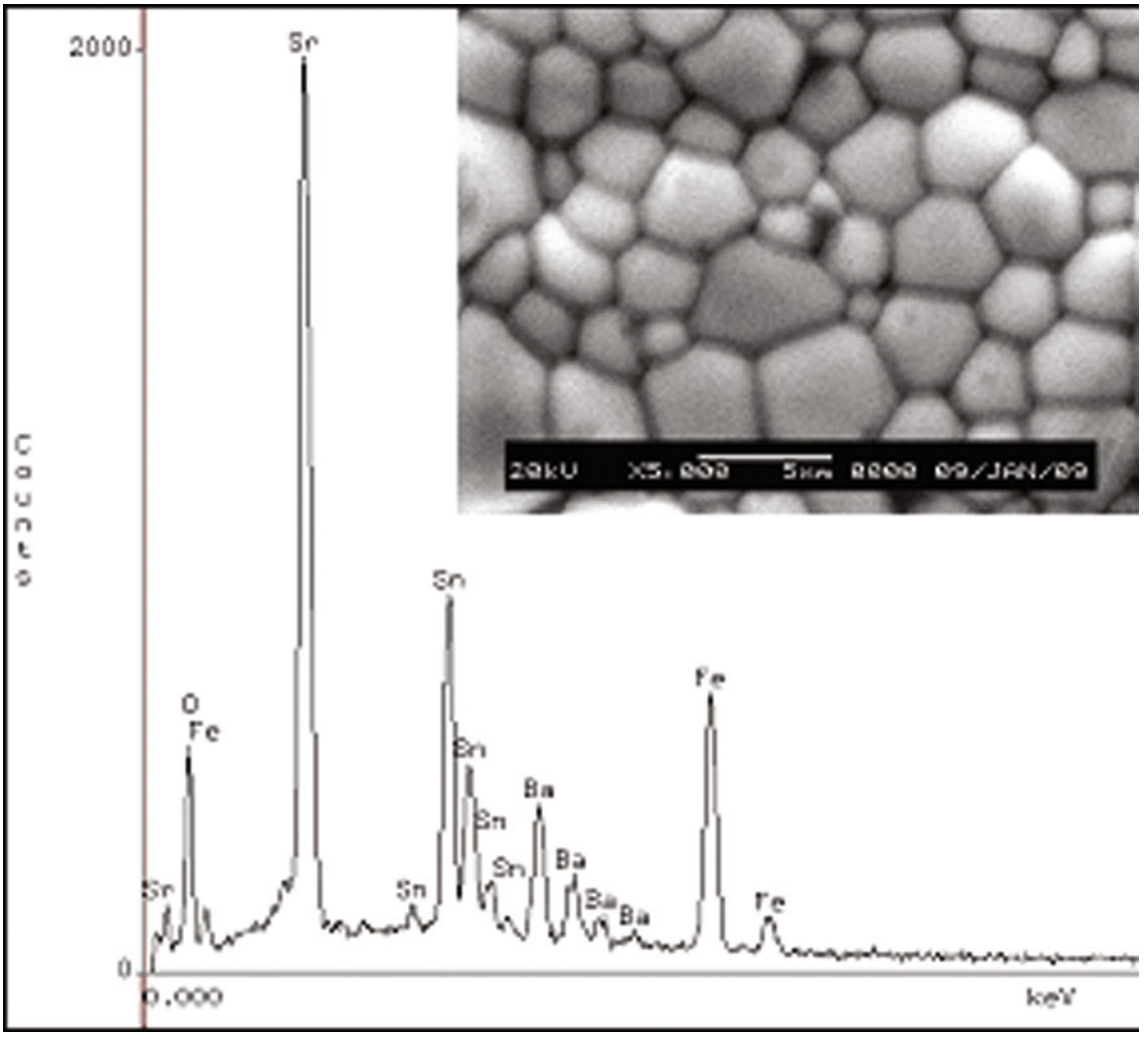

Figure 2. EDS spectra of composition, $x = 0{\cdot}8$. Inset shows SEM microphotograph of $Sr_{0\cdot8}Ba_{0\cdot2}Fe_{0\cdot6}Sn_{0\cdot4}O_{3-\varepsilon}$ ceramic.

temperature ($1/T$). The thermistor constants were calculated using the Arrhenius-type equations (Macklen 1979):

$$B_{298/358} = \frac{\ln\left(\rho_{298}/\rho_{358}\right)}{T_{298}^{-1} - T_{358}^{-1}}, \tag{2}$$

$$E_a = B \cdot k_B, \tag{3}$$

where ρ_{298} and ρ_{358} are the measured electrical resistivity at absolute temperature, T_{298} (298 K) and T_{358} (358 K), respectively and k_B the Boltzmann constant. The values of ρ_{298}, $B_{298/358}$ and activation energy (E_a), as summarized in table 2, are in the range of 0·37–11·0 kΩ·cm, 2466–3703 K and 0·212–0·319 eV, respectively. The room temperature resistivity of all the samples decreases with the increase of Sr content. The reason for this behaviour can

Table 1. Atomic ratio and $3-\varepsilon$ value calculated by EDS analysis.

Compositions (x)	Elements/atom%					($3-\varepsilon$) value
	Ba	Sr	O	Sn	Fe	
$x = 0{\cdot}2$	3·56	15·02	60·41	8·18	12·83	2·875
$x = 0{\cdot}4$	7·25	11·34	60·33	8·36	12·72	2·861
$x = 0{\cdot}5$	9·78	9·57	59·74	8·67	12·24	2·857
$x = 0{\cdot}6$	11·81	8·02	59·27	8·60	12·30	2·835
$x = 0{\cdot}8$	15·24	4·55	58·58	8·75	12·88	2·708

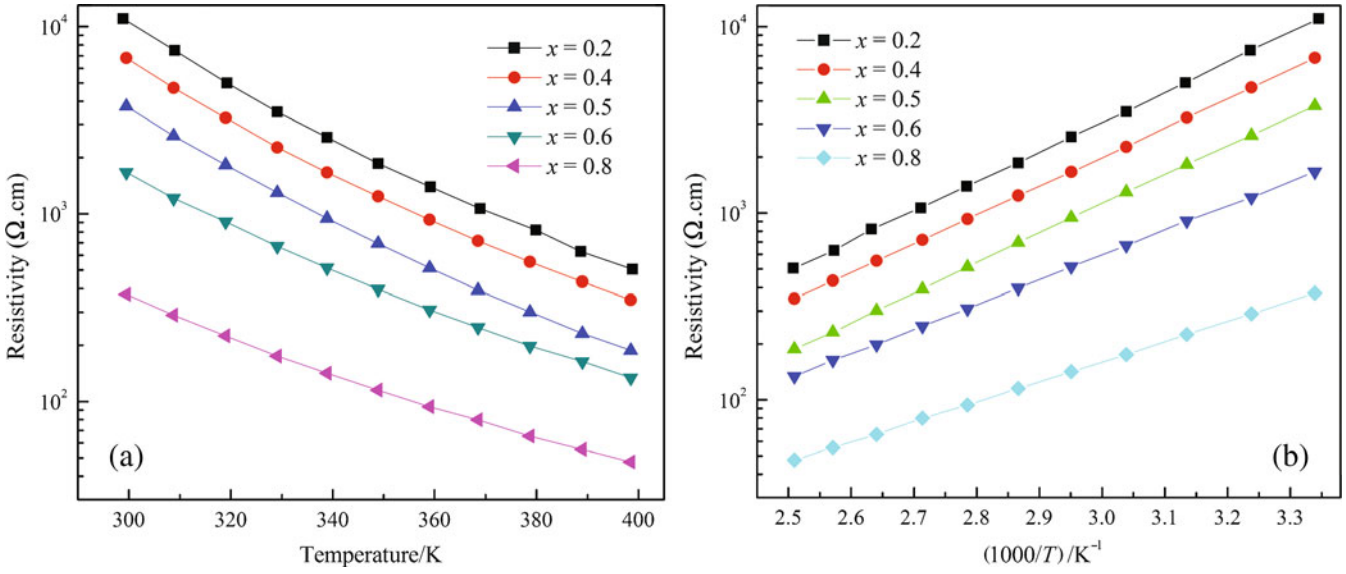

Figure 3. (**a**) Relationship between electrical resistivity (ρ) and absolute temperature (T) for $Sr_xBa_{1-x}Fe_{0.6}Sn_{0.4}O_{3-\varepsilon}$ ($0{\cdot}2 \leq x \leq 0{\cdot}8$) ceramics and (**b**) relationship between logarithmic ρ and reciprocal of absolute temperature ($1/T$) for $Sr_xBa_{1-x}Fe_{0.6}Sn_{0.4}O_{3-\varepsilon}$ ($0{\cdot}2 \leq x \leq 0{\cdot}8$) ceramics.

Table 2. Sintered temperatures resistivity at 298 K, $B_{298/358}$ constant and activation energy of prepared $Sr_xBa_{1-x}Fe_{0.6}Sn_{0.4}O_{3-\varepsilon}$ ($0{\cdot}2 \leq x \leq 0{\cdot}8$) NTC thermistors.

Compositions (x)	Sintered temperatures (°C)	Resistivity at 298 K (kΩ·cm)	$B_{298/358}$ constant (K)	Activation energy (eV)
$x = 0{\cdot}2$	1300	11·04	3703	0·319
$x = 0{\cdot}4$	1290	6·810	3561	0·307
$x = 0{\cdot}5$	1280	3·760	3557	0·306
$x = 0{\cdot}6$	1280	1·666	3015	0·259
$x = 0{\cdot}8$	1280	0·373	2466	0·212

be attributed to the nature of substituting Sr. It is reported that the introduction of Sr in $BaFeO_{3-\varepsilon}$ ceramic leads to the decrease of Fe–O band and thus to the conductivity improvement of electronic conduction from electronic transport of the Fe(IV)–O–Fe(IV) chains (Hombo *et al* 1990). In the above XRD analysis of $Sr_xBa_{1-x}Fe_{0.6}Sn_{0.4}O_{3-\varepsilon}$ ceramics, the lattice parameters also decrease with increasing Sr content. This means that the $Sr_xBa_{1-x}Fe_{0.6}Sn_{0.4}O_{3-\varepsilon}$ thermistors show a similar behaviour like $BaFeO_{3-\varepsilon}$ ceramic (Hombo *et al* 1990), i. e. the electronic conductivity of $Sr_xBa_{1-x}Fe_{0.6}Sn_{0.4}O_{3-\varepsilon}$ ceramics can be enhanced with the increase of Sr content. Furthermore, the oxygen vacancy concentration of $Sr_xBa_{1-x}Fe_{0.6}Sn_{0.4}O_{3-\varepsilon}$ increases with the rise of Sr content. It is well known that the existence of oxygen vacancy in $Sr_xBa_{1-x}Fe_{0.6}Sn_{0.4}O_{3-\varepsilon}$ ceramics can also improve ionic conductivity (Kharton *et al* 2002). Thus, the total conductivity of $Sr_xBa_{1-x}Fe_{0.6}Sn_{0.4}O_{3-\varepsilon}$ ceramics increases with the increase of Sr content.

Various attempts have been made to explain the NTC effect and a.c. complex impedance methods that are widely used to characterize electronic materials. The output response of such a measurement in a complex plane plot appears in the form of a succession of semicircles. The high- and low-frequency semicircle arcs generally represent the bulk contribution and grain boundary contribution, respectively. In order to analyse or interpret experimental data and each contribution, it is essential to have an equivalent circuit model that provides a realistic representation of the electrical properties. In electronic materials, it is necessary to include an extra impedance element representing ceramic–electrode interface (Heinen and Waser 1998). A series of arrangement of three parallel-*RC* components is used to represent the grain, grain boundary and ceramic–electrode interface in the Ag-coated polycrystalline materials. In reality, few systems behave in a perfect Debye manner as represented by ideal resistors (R) and capacitors (C), in circuit model, C is usually substituted by the non-ideal capacitance-constant phase element (CPE) (Rachna *et al* 2008).

For the thermistor ceramics with composition $x \leq 0{\cdot}4$, we employ the complex plane impedance to analyse the interior

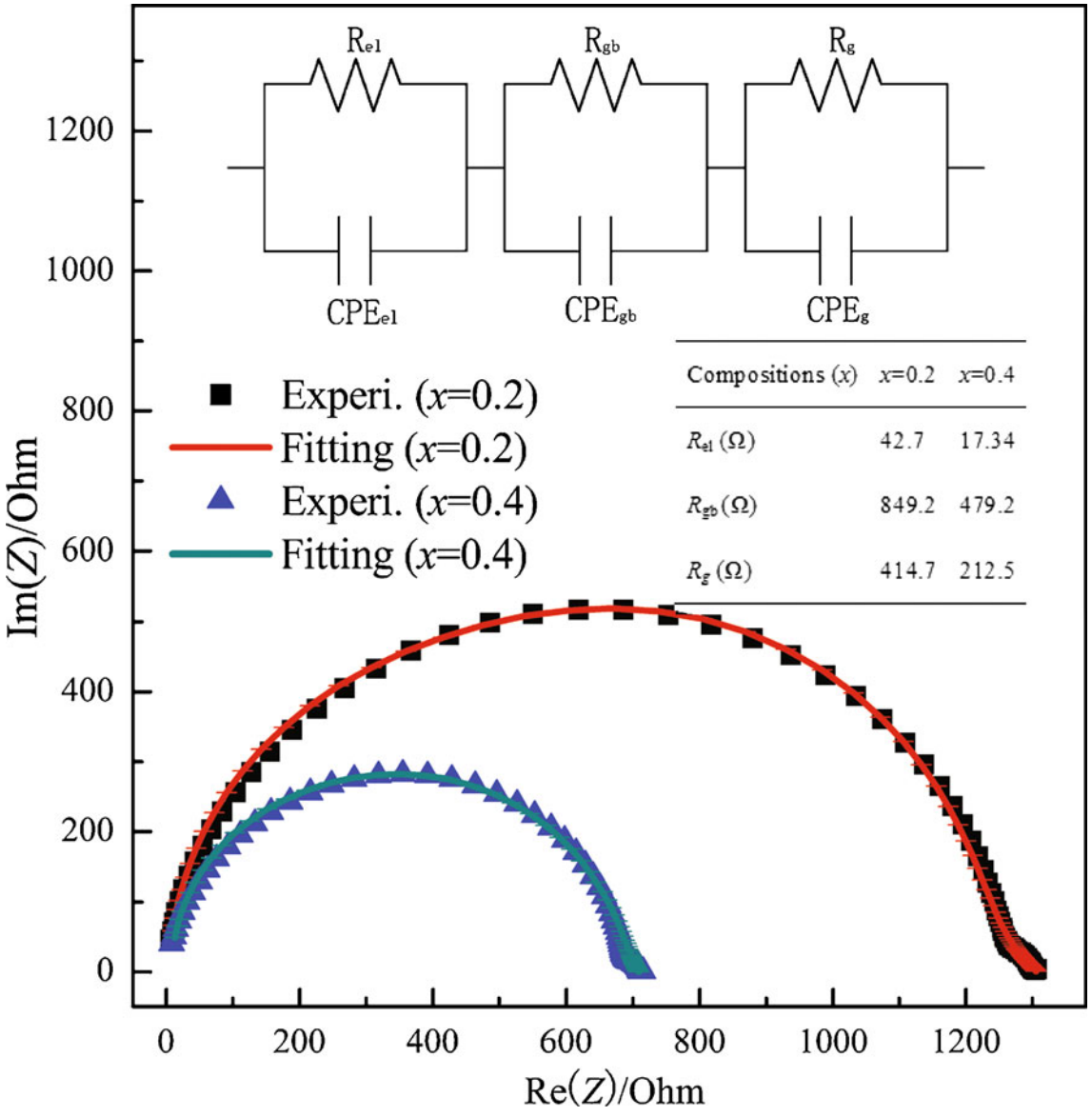

Figure 4. Impedance diagrams of $Sr_xBa_{1-x}Fe_{0.6}Sn_{0.4}O_{3-\varepsilon}$ ($x = 0{\cdot}2$ and $0{\cdot}4$) samples at 298 K. Inset represents equivalent circuit model.

characteristics. The typical complex plane impedance plots are shown in figure 4. Two semicircular arcs are observed respectively in the two samples, the small arc is in low frequency range and the large arc is in high frequency range. Based on the shape of impedance diagrams and frequency region of semicircles or arcs, we deduce that for the compositions with $x = 0{\cdot}2$ and $0{\cdot}4$, the equivalent circuit (as shown in the inset of figure 4) is composed of three components corresponding to grain boundary ($R_{gb}CPE_{gb}$), grain (R_gCPE_g) and ceramic–electrode interface ($R_{el}CPE_{el}$), respectively. The fitted impedance data by the equivalent circuit are also shown in figure 4. From figure 4, it is seen that the fitting lines are in good agreement with the experimental data. The fitting results of various electrical resistances are shown in inset table of figure 4. From the inset table, it is observed that the magnitude of total electrical resistance is mainly determined by R_g and R_{gb}.

Complex impedance spectra of $Sr_{0.4}Ba_{0.6}Fe_{0.6}Sn_{0.4}O_{3-\varepsilon}$ at different temperatures, shown in figure 5, are also found to have the same two semicircular arcs as the impedance diagram of $Sr_{0.4}Ba_{0.6}Fe_{0.6}Sn_{0.4}O_{3-\varepsilon}$ ceramic at 298 K. Thus, the impedance data at different temperatures can be fitted by the equivalent circuit in the inset of figure 4. The electrical resistance of grain and grain boundary, extracted at temperatures 303−343 K by nonlinear least square fitting method, are depicted in the inset of figure 6(b). At temperatures $T \leq 328$ K, the grain boundary resistance gradually decreases with increasing temperature and the grain resistance slowly changes. At higher temperatures ($T > 328$ K), the value of grain boundary resistance decreases to about 100 Ω and tends

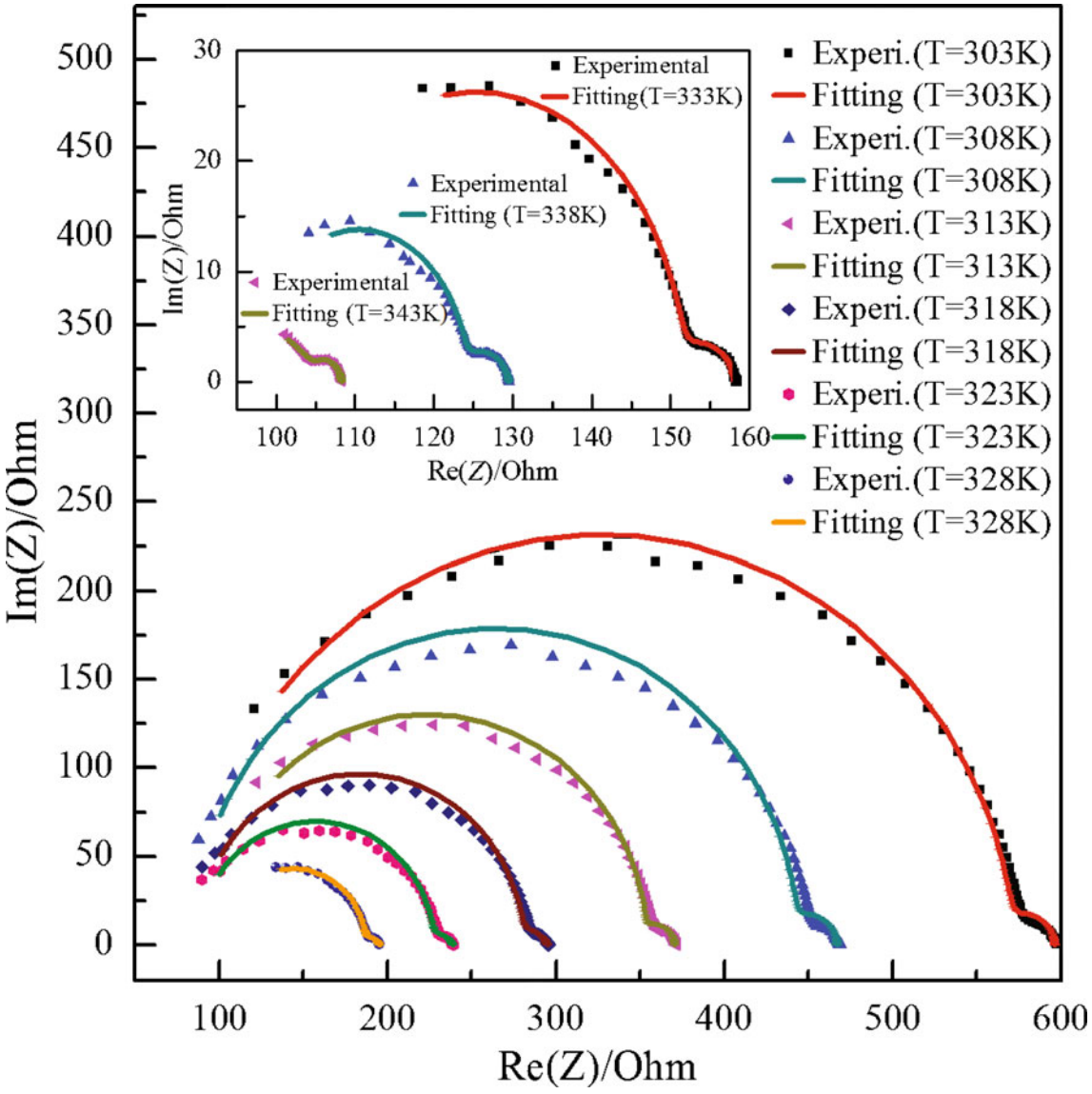

Figure 5. Impedance diagrams of $Sr_{0.4}Ba_{0.6}Fe_{0.6}Sn_{0.4}O_{3-\varepsilon}$ ceramic at different temperatures.

to be steady. Furthermore, it can be seen that the values of resistance R_{el} are basically a constant, irrespective of the temperature change.

The imaginary parts of electric modulus (Im(M)) and electrical resistance (Im(Z)) of the $Sr_{0.4}Ba_{0.6}Fe_{0.6}Sn_{0.4}O_{3-\varepsilon}$ ceramic, as a function of logarithmic frequency at different temperatures, are shown in figures 6(a) and (b), respectively. Im(M) is calculated by the following equation:

$$\mathrm{Im}\,(M) = -jC_0\omega \mathrm{Re}\,(Z), \tag{4}$$

where C_0 is the vacuum capacitance of the cell, ω the angular frequency ($2\pi f$) and Re(Z) the real part of electrical resistance. Figure 6a represents the impedance loss spectrum (Im(Z)$-f$) of the $Sr_{0.4}Ba_{0.6}Fe_{0.6}Sn_{0.4}O_{3-\varepsilon}$ thermistor at different temperatures. The nature of the pattern is characterized by: (i) a small hump at low frequency range and a clear peak in higher frequency range and (ii) an obvious decrease in the height of the peak at higher frequency and the shift to higher frequencies with rise in temperature, such a behaviour indicates the reduction of impedance relaxation time in the system. In figure 6b, the peak of Im(M) curves tends to shift to higher frequency with increasing temperature. These phenomena indicate that the relaxation time of electric modulus is also shortened with temperature. The characteristics from figures 6(a) and (b) indicate that atleast three relaxation processes existed in the ceramic materials. The small humps and clear peaks of figure 6(a) are attributed to the relaxation process of ceramic–electrode interface and grain boundary, respectively. For each curves of figure 6(b), the only peak observed in the limited frequency range is the contribution of grain relaxation. Although some peaks are not observed due to the limiting frequency range, the unobserved peaks are still attributed to the grain contribution. The unob-

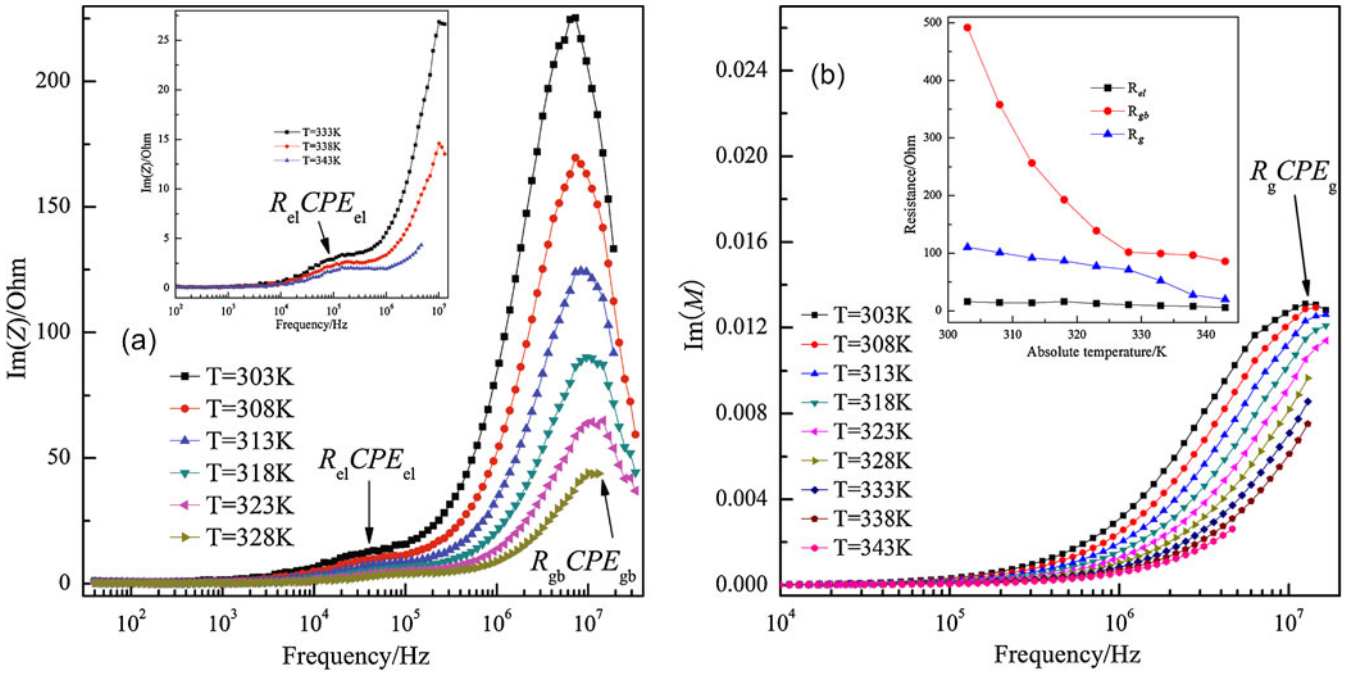

Figure 6. Variation of (**a**) Im(Z) and (**b**) Im(M) with frequency at different temperatures for composition $x = 0{\cdot}4$. Inset of figure 6(b) shows values of resistance R_{gb}, R_g and R_{el}, as a function of absolute temperature, T.

served peaks are also reported in literature (Li *et al* 2009). It can be observed that the peak frequency of Im(Z) and Im(M) curves, corresponding to the grain boundary, show complete mismatch ($f_{\mathrm{Im}(Z)} < f_{\mathrm{Im}(M)}$) at various temperatures. The difference of peak frequency between Im(Z) and Im(M) curves is an obvious evidence of delocalized conduction or indicative of short-range conduction mechanism (Nobre and Lanfredi 2003).

4. Conclusions

The sintered $Sr_xBa_{1-x}Fe_{0\cdot6}Sn_{0\cdot4}O_{3-\varepsilon}$ ($0{\cdot}2 \leq x \leq 0{\cdot}8$) bodies are solid solutions with cubic perovskite structure. The lattice parameter, a and the oxygen vacancy are affected by the substituted Sr at Ba-site. The values of ρ_{298}, $B_{298/358}$ and E_a of NTC thermistors are in the range of 0·37–11·0 kΩ·cm, 2466–3703 K and 0·212–0·319 eV, respectively. The room temperature resistivity decreases with increasing Sr content. Based on impedance analysis, it is found that the total electrical resistance of the measured NTC thermistors is composed of grain resistance, grain boundary resistance and resistance of ceramic–electrode interface. The thermistor behaviour of NTC ceramics is mainly attributed to grain boundary. For the compositions with $x = 0{\cdot}2$ and 0·4, there are a series of arrangement of three parallel *RCPE* components in the ceramics associated with grain, grain boundary and ceramic–electrode interface. For the composition with $x = 0{\cdot}4$, the mismatch between the peaks of Im(Z) and Im(M) curves at various temperatures suggests the presence of localized conduction or short-range conduction mechanism.

References

Cerdà J, Arbiol J, Dezanneau G, Díaz R and Morante J R 2002 *Sensor Actuator* **B84** 21

Hadjarab B, Bouguelia A, Benchettara A and Trari M 2008 *J. Alloys Compd.* **461** 360

Heinen B and Waser R 1998 *J. Mater. Sci.* **33** 4603

Hombo J, Matsumoto Y and Kawano T 1990 *J. Solid State Chem.* **84** 138

Kharton V V *et al* 2002 *Solid State Ionics* **150** 229

Kocemba I, Jedrzejewska M W, Szychowska A, Rynkowski J and Głowka M 2007 *Sensor Actuator* **B121** 401

Kumar A, Singh B P, Choudhary R N P and Thakur A K 2005a *J. Alloys Compd.* **394** 292

Kumar A, Singh B P, Choudhary R N P and Thakur A K 2005b *Mater. Lett.* **59** 1880

Kumar A, Choudhary R N P, Singh B P and Thakur A K 2006a *Ceram. Int.* **32** 73

Kumar A, Singh B P, Choudhary R N P and Thakur A K 2006b *Mater. Chem. Phys.* **99** 150

Li M, Feteira A and Sinclair D C 2009 *J. Appl. Phys.* **105** 114109

Lu W Z, Jiang S L, Zhou D X and Gong S P 2000 *Sensor Actuator* **80** 35

Macklen E D 1979 *Thermistors* (Ayr, Scotland: Electrochemical Publications Ltd)

Maekawa T, Kurosaki K and Yamanaka S 2006 *J. Alloys Compd.* **416** 214

Nobre M A L and Lanfredi S 2003 *J. Phys. Chem. Solids* **64** 2457

Rachna S, Gupta S M and Bhattacharyya S 2008 *Indian Acad. Sci.* **72** 599

Yuan C L, Liu X Y, Yang Y and Zhou C R 2010 *J. Mater. Sci.* **45** 2681